de Haas–van Alphen effect in the Ti-doped CsV_3Sb_5 kagome compound under magnetic fields up to 41 Tesla

Kyryl Shtefiienko,[1] Tucker Beekmann,[1] Matthew J. Stitz,[2] Ganesh Pokharel,[2] Stephen D. Wilson,[3] Christopher A. Mizzi,[4] David E. Graf,[5,6] and Keshav Shrestha[1,*]

[1]*Department of Chemistry and Physics, West Texas A & M University, Canyon, Texas 79016, USA*
[2]*Perry College of Mathematics, Computing, and Sciences, University of West Georgia, Carrollton, Georgia 30118, USA*
[3]*Materials Department, University of California, Santa Barbara, California 93106, USA*
[4]*National High Magnetic Field Laboratory, Los Alamos National Laboratory, Los Alamos, New Mexico 87545, USA*
[5]*National High Magnetic Field Laboratory, Tallahassee, Florida 32310, USA*
[6]*Department of Physics, Florida State University, Tallahassee, Florida 32306, USA*

(Received 30 June 2025; revised 10 November 2025; accepted 19 December 2025; published 9 January 2026)

The recently discovered kagome superconductor CsV_3Sb_5 exhibits a rich interplay between superconductivity (SC) and charge density wave order, both of which are highly tunable via doping or pressure. In particular, hole doping CsV_3Sb_5 by substituting vanadium with the relatively smaller titanium allows controlled tuning of the correlated phases, revealing two distinct superconducting domes (SC I and SC II) across the doping range. A prior tunneling experiment [H. Yang, *et al.*, Sci. Bull. **67**, 2176 (2022)] suggests differing SC pairing symmetries between the two domes. Since the Fermi surface topology—including features such as pockets, nesting vectors, and dimensionality—plays a crucial role in determining the superconducting pairing mechanism, we investigate its evolution in $CsTi_xV_{3-x}Sb_5$ across four doping levels ($x = 0$, 0.03, 0.10, and 0.15), spanning both SC domes. High-field torque magnetometry up to 41 T reveals pronounced de Haas–van Alphen (dHvA) oscillations, with distinct frequency spectra observed in SC I and SC II, implying that these SC domes have different electronic and Fermi surface properties. First-principles calculations using density functional theory also show changes in key electronic features—such as Dirac crossings, van Hove singularities, and flat bands—when vanadium is replaced with titanium. Notably, the Fermi surface topology shows clear deformation with increasing titanium doping. Our experimental and theoretical results provide compelling evidence for distinct Fermi surface characteristics in the SC I and SC II regions, offering insights into the possible existence of different pairing mechanisms across the two superconducting domes in $CsTi_xV_{3-x}Sb_5$.

DOI: 10.1103/871s-2rsl

I. INTRODUCTION

In recent years, materials with kagome lattice structures—especially those made of corner-sharing patterns—have gained a lot of attention because they show interesting quantum states [1–4]. These include superconductivity (SC), charge density wave (CDW) order, nontrivial band topology, and magnetically frustrated ground states [5–7]. Scientists have discovered several types of kagome materials [6,8–14] made with titanium and vanadium, which help explore new quantum and topological properties. Among these, the AV_3Sb_5 compounds (A = K, Rb, Cs), collectively referred to as the 135 family, are particularly notable for their unique structural and electronic properties [8,9]. These materials crystallize in a hexagonal lattice with the $P6/mmm$ space group. Within this structure, the vanadium atoms form a two-dimensional (2D), corner-sharing kagome network [Fig. 1(a)], leading to a complex interplay between electronic correlations and topological effects. Members of this family exhibit SC with critical temperature $T_c \approx 0.9$–3 K, coexisting with a CDW phase near $T^* \approx 90$–110 K. Their electronic band structures are marked by several features of interest, including flat bands, Dirac crossings, and van Hove singularities situated near the Fermi level [15–18].

Furthermore, AV_3Sb_5 exhibits nontrivial band topology, as confirmed by quantum oscillation studies [19–22] and by topological invariant $\mathbf{Z}_2$ calculations [9,18] using density functional theory (DFT). The coexistence of nontrivial topology and superconductivity in these systems makes them promising candidates for topological superconductors that can host Majorana quasiparticles. A tunneling spectroscopy experiment on CsV_3Sb_5 has reported the presence of a zero-bias conductance peak, supporting the possibility that this material is a topological superconductor [23].

External perturbations such as doping or pressure serve as powerful tools for inducing or tuning the intrinsic electronic properties of quantum materials [24,25]. These perturbations primarily change interatomic distances and/or carrier concentrations, which in turn modifies electronic interaction strengths and ultimately influences the material's electronic behavior. This approach has been widely applied across various systems; for instance, carrier doping in cuprates induces

*Contact author: kshrestha@wtamu.edu

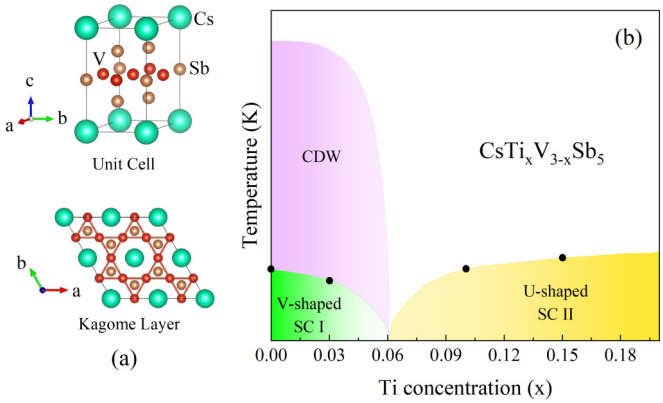

FIG. 1. (a) Unit cell (top) and kagome layer (bottom) of the CsV_3Sb_5 compound. (b) A schematic phase diagram, adapted from Ref. [32], showing charge density wave (CDW) and superconducting (SC) phases for $CsTi_xV_{3-x}Sb_5$ with varying x. The CDW phase is gradually suppressed with x and vanishes at the critical doping $x_c = 0.06$. There are two superconducting phases: the V-shaped SC I and the U-shaped SC II [33]. Dot symbols indicate the four doping levels ($x = 0$, 0.03, 0.10, and 0.15) examined in this study.

SC, while in iron-based superconductors, applied pressure suppresses magnetic order and induces SC [26–31].

The kagome metal AV_3Sb_5 has recently emerged as a compelling platform for investigating doping and pressure-tuned quantum phenomena, owing to its complex interplay of SC, CDW order, and nontrivial topology [32–39]. Intriguingly, physical pressure induces a nonmonotonic evolution of T_c, resulting in an M-shaped T-versus-pressure phase diagram with two distinct critical points at $P_{c1} \approx 0.7$ GPa and $P_{c2} \approx 2$ GPa [40–45]. Interestingly, the similar phase diagram can be reproduced by substituting vanadium with the relatively smaller titanium atom [32,33], which introduces both hole doping and a modest degree of chemical pressure. Notably, the Ti-doped phase diagram closely resembles that of Sn-doped $CsV_3Sb_{5-x}Sn_x$ [38,46]—another hole-doped system—suggesting that hole doping is the dominant effect of Ti substitution in $CsTi_xV_{3-x}Sb_5$, while lattice contraction due to chemical pressure plays a secondary role. Ti-doped CsV_3Sb_5 exhibits suppression of the CDW phase and the emergence of two superconducting domes, SC I and SC II, separated by a critical doping level of $x_c = 0.06$ (see Fig. 1).

The tunneling spectroscopy experiments [33] show clear differences in the current-voltage (I-V) behavior between the two superconducting regions. The SC I region shows a V-shaped curve, while SC II shows a U-shaped one, suggesting that the two regions may have different types of superconducting pairing. The electronic structure—especially the shape of the Fermi surface—plays an important role in superconductivity and may help explain the differences between the two domes. In this study, we examined the Fermi surface of $CsTi_xV_{3-x}Sb_5$ in both SC I and SC II by using torque magnetometry in very strong magnetic fields (up to 41 T). We observed clear de Haas–van Alphen (dHvA) oscillations, with frequencies up to 4000 T when the magnetic field is applied along the c axis of the sample. These frequencies were different between SC I and SC II: for example, high-frequency signals seen in SC I were missing in SC II. This suggests that the electronic structures of the two regions are distinct. Our DFT calculations also show that titanium doping modifies the band structure and the shape of the Fermi surface, which qualitatively helps explain the experimental observations.

II. EXPERIMENTAL AND COMPUTATIONAL DETAILS

High-quality single crystals of Ti-substituted CsV_3Sb_5 were synthesized using a standard self-flux method. The details of sample synthesis are described in our recent publication [47]. After growth, the shiny, platelike crystals were manually extracted from the residual flux under ambient conditions and rinsed with ethanol to remove any surface contaminants. These crystals exhibited moderate air stability for brief exposures. The structural integrity and compositional uniformity of the samples were assessed through powder x-ray diffraction and scanning electron microscopy. Elemental analysis via energy-dispersive spectroscopy confirmed the targeted stoichiometry and successful incorporation of Ti into the crystal lattice.

Resistivity measurements were performed using a standard four-wire configuration with a Quantum Design Physical Property Measurement System (PPMS). Torque measurements were carried out using a piezoresistive cantilever setup at the National High Magnetic Field Laboratory (NHMFL) in Tallahassee, Florida. A tiny single crystal of $CsTi_xV_{3-x}Sb_5$ was selected, mounted onto the cantilever arm with vacuum grease, and then attached to the rotatable sample platform for angular-dependent measurements.

First-principles calculations for $CsTi_xV_{3-x}Sb_5$ were performed using both WIEN2K [48,49] and the open-access, DFT-based computational package QUANTUM ESPRESSO (QE) [50–52]. The unit cell structure was initially optimized using the vc-relax algorithm in QE, combined with conjugate gradient (CG) diagonalization. Subsequent calculations of the electronic band structure and Fermi surface were carried out using WIEN2K. The exchange-correlation effects were treated within the generalized gradient approximation (GGA), as formulated by Perdew, Burke, and Ernzerhof (PBE) [53]. Self-consistent field (SCF) calculations were converged to an energy threshold of 10^{-4} Rydbergs. The atomic sphere radii (RMT) were uniformly set to 2.50 Bohr for Cs, V, Ti, and Sb atoms. To achieve high-resolution Fermi surface mapping, a dense Monkhorst-Pack **k**-point mesh of $25 \times 25 \times 12$ was employed. The effect of Ti substitution was modeled by replacing a single V atom with Ti in the conventional unit cell, effectively simulating hole doping; this simplified approach captures the qualitative evolution of the Fermi surface in a rigid-band-like manner, although it does not fully reproduce the disorder or local potential variations present in partially substituted samples. Theoretical quantum oscillation frequencies were subsequently extracted using the SKEAF code [54].

III. RESULTS AND DISCUSSION

Figure 2 shows the temperature dependence of electrical resistance, $R(T)$, for $CsTi_xV_{3-x}Sb_5$. The undoped sample exhibits typical metallic behavior, with a high residual resistance ratio (RRR = 60), indicating good crystal quality. This value

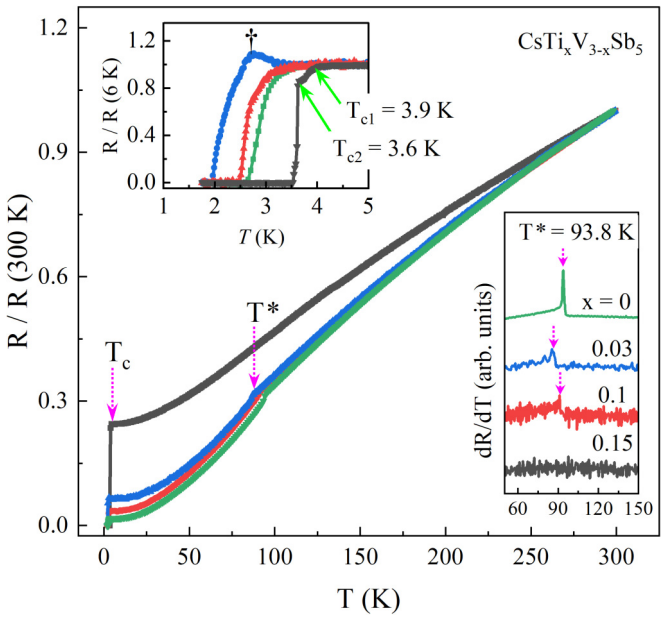

FIG. 2. Temperature dependence of the normalized electrical resistance $R(T)$ for $CsTi_xV_{3-x}Sb_5$ with $x = 0$, 0.03, 0.10, and 0.15. The resistance decreases with decreasing temperature and exhibits two distinct transitions: a charge density wave (CDW) transition near $T^* \approx 90$ K and a superconducting (SC) transition near $T_c \approx 3$ K. Top inset: Zoomed-in view of $R(T)$ below 6 K, emphasizing the SC transition. A humplike feature appears before the superconducting transition, marked by the dagger symbol. Bottom inset: First derivative dR/dT near 90 K, highlighting the CDW transition. The CDW feature is barely visible at $x = 0.10$ and is completely absent at $x = 0.15$. The curves are shifted for clarity.

is similar to that previously reported for CsV_3Sb_5 [9]. As more Ti is added, the RRR decreases to 29, 16, and 4 for $x = 0.03$, 0.10, and 0.15, respectively. This reduction in RRR suggests that Ti doping introduces increased disorder and scattering, which hinders electron transport in the material. The $R(T)$ curve displays two distinct transitions: one near $T^* \approx 90$ K, associated with the CDW phase, and another near $T_c \approx 3$ K, corresponding to the onset of superconductivity. The CDW transition is more clearly visible in the derivative curve shown in the lower inset. For the parent compound ($x = 0$), the CDW transition is sharp and occurs at $T^* = 93.8$ K, closely matching the previously reported value of 94 K [9]. The CDW transition is absent at $x = 0.15$. It is worth noting that even at $x = 0.10$, a subtle signature of the CDW transition remains visible in the first derivative of $R(T)$. According to previous phase diagram studies [32,33,37], the CDW phase is expected to vanish above the critical doping level of $x_c = 0.06$. One possible explanation is that the $x = 0.10$ sample is not fully homogeneous and may retain a small fraction of the parent compound as a minority phase.

The top inset in Fig. 2 shows a zoomed-in view of the $R(T)$ curves below 6 K. For $x = 0$, the superconducting transition temperature is $T_c = 3.6$ K, which is slightly higher than previously reported values of 2.5–2.8 K [9,55,56], but consistent with the 3.5 K reported in Ref. [20]. Interestingly, T_c exhibits a nonmonotonic dependence on x: it first decreases and then increases again, resembling the phase diagram shown in Fig. 1(b). This behavior, along with the suppression of the CDW phase, is consistent with previous doping studies [32–39,57].

Moreover, a closer inspection of the transition reveals the appearance of two superconducting transition-like features upon Ti doping. For example, at $x = 0.15$, two distinct transitions are observed at $T_{c1} = 3.6$ K and $T_{c2} = 3.9$ K, as indicated by the solid arrows (Fig. 2, top inset). Additionally, we observe a shallow upturnlike feature just below T_c for $x = 0.03$. Similar features have also been observed in highly Ti-doped CsV_3Sb_5 samples [32,33], although they were not explicitly discussed in those works. In our samples, the RRR decreases systematically with increasing Ti concentration, indicating enhanced scattering due to disorder or local compositional fluctuations introduced by Ti substitution. The appearance of two superconducting transitions for $x = 0.15$ may therefore reflect the presence of regions with slightly different local Ti concentrations or superconducting properties. Although detailed structural or microscopic analyses were not performed in this study, such inhomogeneity could plausibly account for the observed resistive anomalies near T_c. Further investigations using high-resolution structural probes would be valuable to confirm this interpretation.

To probe the electronic structure across the two superconducting domes, we performed torque magnetometry measurements in magnetic fields up to 41 T, as shown in Fig. 3(a). The torque signal measured at 0.4 K begins to exhibit dHvA oscillations above 20 T. These oscillations are observed in all four samples and appear to consist of multiple frequencies. To extract the frequency components, we subtracted a second-order polynomial background from the data above 20 T and then performed a Fourier transform. The oscillations are more clearly visible in the background-subtracted data, as shown in the inset. Figure 3(b) displays the resulting frequency spectra corresponding to the data in Fig. 3(a). The spectra look similar for all doping levels. There exist seven distinct peaks at $F_\alpha = 105$, $F_\beta = 734$, $F_\chi = 786$, $F_\gamma = 1375$, $F_\delta = 2066$, $F_\phi = 2962$, and $F_\lambda = 4180$ T. A peak near 208 T, indicated by the asterisk, is nearly twice that of F_α, suggesting it is the second harmonic. The lower-frequency signals, especially F_χ, are more prominent than the higher-frequency components. Previous high-field torque measurements [15–17,19,21,58–61] in AV_3Sb_5 have also revealed multiple frequency peaks with a similar spectra, with frequencies reaching as high as 4000 T.

As Ti doping increases, the relative amplitudes and positions of these peaks shift slightly. At the highest doping level ($x = 0.15$), the prominent F_χ peak, along with the high-frequency components F_ϕ and F_λ, disappears. This effect is more clearly visible in the zoomed-in spectrum shown in Fig. 3(b) inset. Since the frequency of quantum oscillations is directly proportional to the cross-sectional area of the Fermi surface [62], the disappearance of certain frequency signals at $x = 0.15$ indicates a change in the electronic structure due to Ti doping. Interestingly, the disappearance of quantum oscillation frequencies with increasing physical pressure has also been observed in our recent experiment [42,63], suggesting that the combined effect of hole doping and chemical pressure,

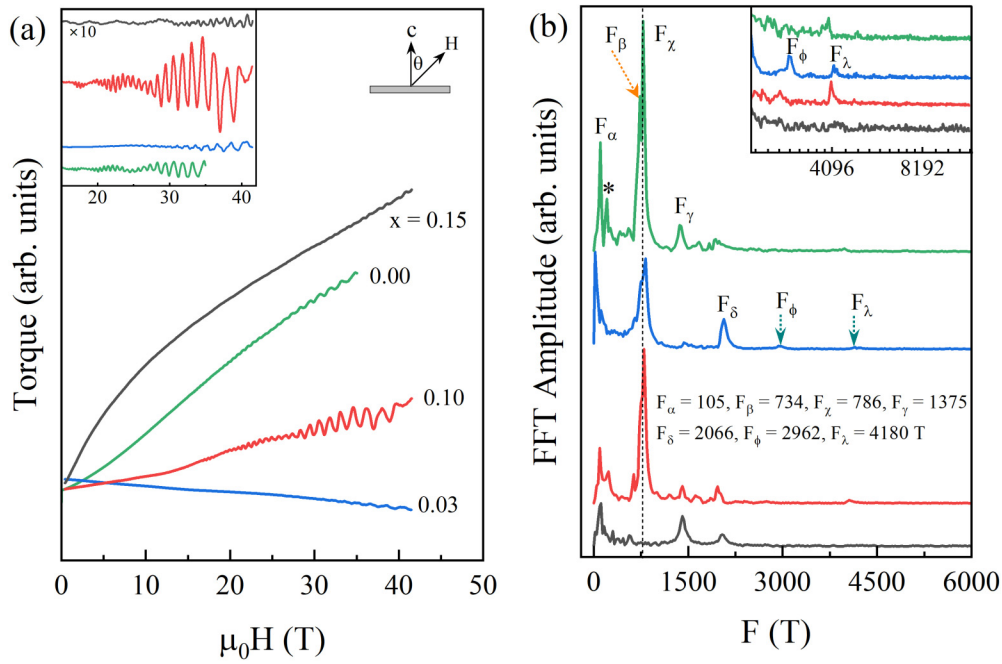

FIG. 3. (a) High-field torque measurements of $CsTi_xV_{3-x}Sb_5$ with $x = 0$, 0.03, 0.10, and 0.15, taken at a tilt angle of $\theta = 0°$ and the base temperature of $T = 0.4$ K. Data for $x = 0$ are included from our previous study (Ref. [15]) for comparison. de Haas–van Alphen (dHvA) oscillations are observed in all samples. Left inset: Background-subtracted torque data. The data for $x = 0.15$ was multiplied by a factor of 10 for better visibility. Right inset: Schematic diagram showing the angle θ between the c axis and the magnetic field H. (b) Corresponding Fourier spectra of the data shown in (a). Multiple frequency peaks are observed at $F_\alpha = 105$, $F_\beta = 734$, $F_\chi = 786$, $F_\gamma = 1375$, $F_\delta = 2066$, $F_\phi = 2962$, and $F_\lambda = 4180$ T. The peak near 208 T, indicated by the asterisk, is the second harmonic of F_α. Notably, F_χ, F_ϕ, and F_λ are absent at $x = 0.15$, as highlighted in the inset.

as well as physical pressure alone, leads to the similar effect, a change in electronic structure—of CsV_3Sb_5.

Figure 4 shows the temperature dependence of the frequency spectra at $\theta = 21°$. At this tilt angle, a new frequency peak, $F_\omega = 2041$ T at $x = 0.03$, emerges, which was not clearly visible in Fig. 3(b). F_ω appears to show an increasing trend at higher x values. The frequency spectrum is very rich, exhibiting nine peaks for $x = 0.03$. The number of peaks, especially those at higher frequencies, decreases with increasing x. At $x = 0.15$, only four peaks—F_α, F_σ, F_ω, and F_δ—can be resolved. Furthermore, as seen in Fig. 4, the amplitude of all peaks diminishes with increasing temperature. As the

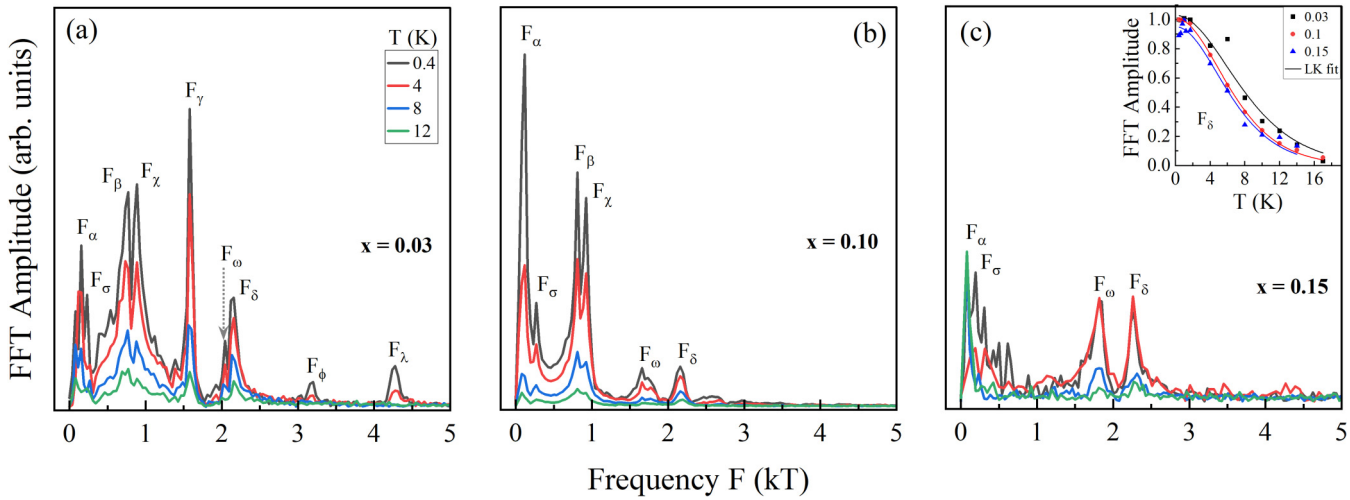

FIG. 4. Quantum oscillation frequency spectra of $CsTi_xV_{3-x}Sb_5$ for (a) $x = 0.03$, (b) $x = 0.10$, and (c) $x = 0.15$, measured at a tilt angle of $\theta = 21°$. The amplitude of all peaks systematically decreases with increasing temperature. For $x = 0.03$, nine prominent peaks are observed, while both the number and positions of the peaks evolve with increasing Ti concentration. At $x = 0.15$, only four peaks remain visible. Inset: Temperature dependence of the amplitude of the F_δ peak for different x values. The scatter points represent experimental data, and the solid lines are best fits using the Lifshitz-Kosevich (LK) Eq. (1).

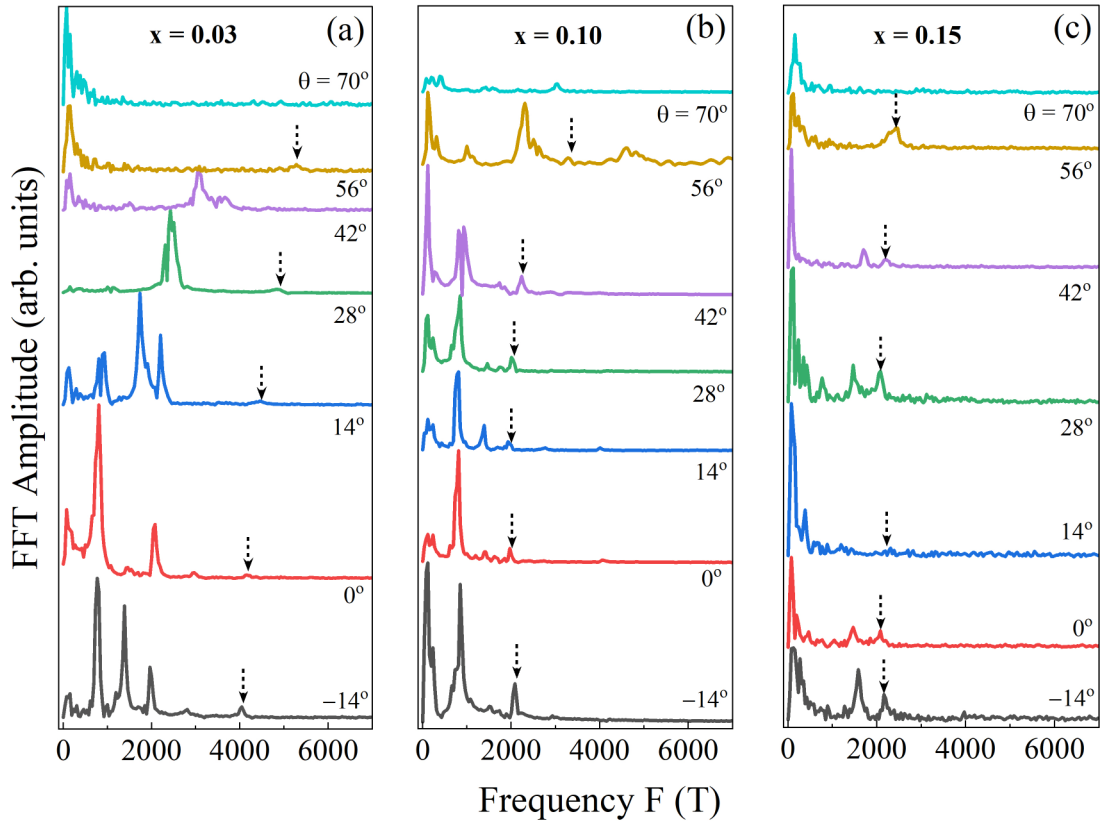

FIG. 5. Angular dependence of the quantum oscillation frequency spectra for $CsTi_xV_{3-x}Sb_5$ at selected tilt angles (θ) for (a) $x = 0.03$, (b) $x = 0.10$, and (c) $x = 0.15$ at $T = 0.4$ K. As θ increases, both the positions and the number of frequency peaks evolve, as highlighted by the dashed arrows. The low-frequency signal near 100 T is observed at all measured angles. Most of the other peaks shift to higher frequencies with increasing θ but vanish above $\theta > 56°$, suggesting a quasi-two-dimensional character of the corresponding Fermi surface sections. The frequency spectra are vertically offset for clarity.

temperature increases, the high-frequency signals disappear more quickly than the lower-frequency ones, indicating higher effective masses associated with those peaks [15,16]. The temperature dependence of frequency can be described by Lifshitz-Kosevich (LK) theory [62,64].

According to LK theory, the temperature and magnetic field dependence of quantum oscillations can be described by

$$\Delta\tau(T,H) \propto e^{-\lambda_D} \frac{\lambda(T/H)}{\sinh[\lambda(T/H)]}, \tag{1}$$

with $\lambda_D(H) = \frac{2\pi^2 k_B}{\hbar e} m^* \frac{T_D}{H}$ and $\lambda(T/H) = \frac{2\pi^2 k_B}{\hbar e} m^* \frac{T}{H}$. Here, T_D, k_B, and m^* represent the Dingle temperature, Boltzmann's constant, and effective mass of the charge carriers, respectively. The first term in the formula is the Dingle factor, which describes the attenuation of the oscillations with field H. The second term explains the decrease in the amplitudes of the oscillations at higher temperatures.

The F_δ peak is present at all Ti-doping levels; therefore, we analyzed its temperature dependence to determine the effective mass, m^*, associated with this peak, as shown in the inset of Fig. 4(c). The scatter points represent the experimental data, while the solid curves correspond to the best fits obtained from the LK formula. As evident from the graph, the LK formula describes the data well. From the fitting parameters, we extracted effective masses of $m^*_\delta = (0.51 \pm 0.03)m_e$, $(0.61 \pm 0.00)m_e$, and $(0.62 \pm 0.03)m_e$ for $x = 0.03$, 0.10, and 0.15, respectively, where m_e is the bare mass of an electron. These values show minimal variation with doping and are comparable to those reported for the parent compound CsV_3Sb_5 [15,19,21].

As shown in Fig. 4, several frequency peaks have been observed in $CsTi_xV_{3-x}Sb_5$. According to Onsager's relation [64,65], the frequency (F) of quantum oscillations is directly proportional to the extremal cross-sectional area (A_F) of the Fermi surface, given by $F = (\hbar/2\pi e)A_F$, where $\hbar$ is the reduced Planck constant and e is the elementary charge. Thus, the quantum oscillation frequency provides as a direct probe of the Fermi surface geometry of the material. By rotating the sample in an applied magnetic field, one can effectively map the shape, size, and topology of the Fermi surface of the material under study [62].

Figure 5 displays the angular dependence of quantum oscillation frequencies for various Ti doping. To improve clarity, the curves are vertically offset, and only selected θ values are shown. As θ increases, most frequency peaks systematically shift to higher values, as marked by the dashed arrows. The quantum oscillation frequencies above 100 T could not be resolved above 56°, suggesting that they originate from quasi-2D orbits. In contrast, a low-frequency peak near

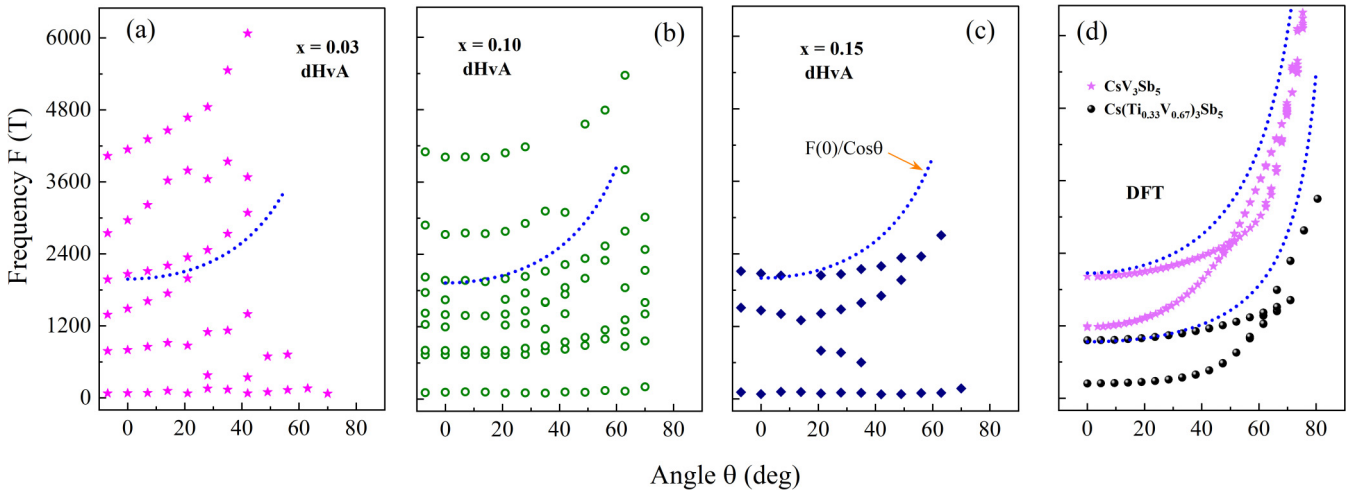

FIG. 6. Angular dependence of quantum oscillation frequencies in $CsTi_xV_{3-x}Sb_5$ for (a) $x = 0.03$, (b) $x = 0.10$, and (c) $x = 0.15$. A low-frequency peak near 100 T remains nearly angle independent, whereas higher-frequency components exhibit an approximately parabolic increase with the tilt angle θ. The dotted curves represent a $F(0)/\cos\theta$ dependence. (d) Theoretical frequencies corresponding to cylindrical Fermi surfaces at the Γ point, calculated using SKEAF code [54] for CsV_3Sb_5 and $Cs(Ti_{0.33}V_{0.67})_3Sb_5$. A clear decrease in the frequency values is observed with Ti doping.

100 T remains nearly constant across all angles, suggesting an almost isotropic pocket. A more detailed angle-resolved analysis for all frequencies is provided in Fig. 6.

Figures 6(a)–6(c) summarize the angular evolution of all detected frequencies for each doping level. As previously noted, samples with $x = 0.03$ and $x = 0.10$ exhibit a large number of frequency peaks extending up to 4000 T. However, for $x = 0.15$, only four distinct peaks are observed, with maximum values near 2000 T. The low-frequency peak around 100 T remains nearly angle independent, while the other peaks increase approximately parabolically with θ. The dashed lines represent fits of the form $F(0)/\cos\theta$, where $F(0)$ is the frequency at $\theta = 0°$, characteristic of a quasi-2D Fermi surface [62,66]. At $x = 0.03$, the experimental data—the frequency signals—seem to closely follow the $F(0)/\cos\theta$ behavior, indicating cylindrical or quasi-2D Fermi surfaces. However, noticeable deviations from quasi-2D behavior appear in the high-frequency signals at higher doping levels ($x = 0.10$ and $x = 0.15$), further suggesting a progressive distortion of the Fermi surface with increasing Ti content. Theoretical frequencies derived from DFT are shown in Fig. 6(d) and will be discussed later.

To interpret the experimental results and gain insight into the changes in the electronic structure induced by Ti doping, we performed electronic band structure and Fermi surface calculations using DFT. To simulate the effect of Ti doping, we replaced one of the vanadium atoms with a titanium atom, corresponding to the composition $Cs(Ti_{0.33}V_{0.67})_3Sb_5$. Figure 7(a) presents the calculated band structures for both pristine CsV_3Sb_5 and Ti-doped $Cs(Ti_{0.33}V_{0.67})_3Sb_5$. The resulting band features are in good agreement with previous electronic structure studies [61,63,67,68]. In the parent compound, several distinctive features are observed near the Fermi level, including multiple Dirac points, van Hove singularities, and a flat band—marked by dotted circles, arrows, and the shaded region, respectively. With Ti doping, these features shift noticeably in energy, indicating that the electronic structure of CsV_3Sb_5 is highly sensitive to the external perturbations such as doping or pressure.

This sensitivity is further illustrated in Fig. 7(b), which displays the corresponding Fermi surfaces. In the parent compound, the Fermi surface features a nearly cylindrical pocket centered at the Γ point and chainlike structures along the Brillouin zone boundaries. Upon Ti doping, the cylindrical feature becomes more constricted with a narrower belly, and the chainlike structures evolve into broader, sheetlike features,

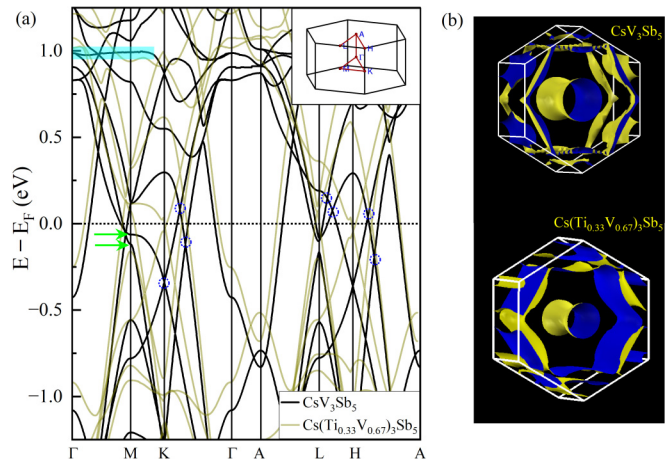

FIG. 7. (a) Electronic band structures of pristine CsV_3Sb_5 and $Cs(Ti_{0.33}V_{0.67})_3Sb_5$. Key features such as the Dirac cone and van Hove singularity shift noticeably with increasing titanium content, as highlighted by arrows and dotted circles. The flat band, highlighted by the shaded region, is absent in $Cs(Ti_{0.33}V_{0.67})_3Sb_5$. Inset: High-symmetry points in the Brillouin zone. (b) Fermi surface of Ti-doped CsV_3Sb_5, illustrating the evolution induced by Ti substitution. The cylindrical feature centered at the Γ point becomes more distorted with doping, while the chainlike structures near the Brillouin-zone boundary evolve into more sheetlike features. An additional small cylindrical Fermi surface also emerges at the zone boundary.

along with the emergence of additional cylindrical Fermi surface at the zone boundary, reflecting significant modifications to the Fermi surface topology.

To examine the quantitative evolution of the theoretical frequencies associated with the Γ-centered Fermi surface, we computed the possible extremal cross sections using the SKEAF code [54], as shown in Fig. 6(d). The calculated frequencies follow an approximate $1/\cos\theta$ dependence, as expected for a quasi-two-dimensional cylindrical Fermi surface. Most importantly, the frequency values systematically decrease with increasing Ti content, consistent with the shrinkage of the Γ-centered Fermi surface at higher Ti doping [Fig. 7(b)].

Because the DFT model employs a single-site Ti substitution corresponding to a higher nominal doping level, a direct quantitative comparison with the experimental frequencies [Fig. 6(a)–6(c)] is not feasible. Nevertheless, the calculations capture the qualitative trend: a reduction of the Γ-centered cylindrical sheet and the emergence of an additional hole-like cylinder at the Brillouin-zone boundary for higher Ti concentrations. Future calculations employing a supercell or virtual crystal approximation (VCA) would enable a closer correspondence to the experimental doping levels and may provide deeper insight into the subtle changes in the electronic structure. Furthermore, the expected low-frequency oscillation from this new Fermi-surface sheet is not experimentally resolved, likely due to enhanced disorder and reduced quantum mobility, which suppress low-frequency components.

It is important to note that, although the evolution of the electronic structure with Ti doping resembles the behavior observed under hydrostatic pressure [42,63], the underlying mechanisms differ. Hydrostatic pressure uniformly compresses the lattice, whereas Ti substitution not only exerts chemical pressure through lattice contraction but also introduces local disorder and modifies the carrier concentration. Consequently, Ti doping leads to both Fermi-surface reconstruction and enhanced scattering effects, which can dampen the quantum oscillation amplitudes.

In the $x = 0.15$ sample, the high-frequency dHvA oscillations (F_ϕ and F_λ) observed in the undoped compound are no longer visible in Fig. 4. This suppression likely arises from two concurrent effects: (i) modification of the Fermi surface due to chemical pressure, as suggested by our DFT calculations, and (ii) increased scattering and disorder associated with higher Ti substitution, which can significantly damp the amplitude of high-frequency oscillations. Therefore, while the disappearance of the F_χ branch may be intrinsic to the Fermi surface change, the absence of the F_ϕ and F_λ peaks cannot be solely attributed to band-structure effects. Both mechanisms likely contribute to the observed behavior. However, given the similarity of the observed evolution of electronic features with our recent studies [42,63] under hydrostatic pressure in CsV_3Sb_5, the chemical pressure effect appears more crucial than the disorder-induced damping due to Ti substitution.

IV. SUMMARY

In summary, we have investigated the evolution of the Fermi surface in Ti-doped kagome metal CsV_3Sb_5 using high-field torque magnetometry and first-principles calculations. This compound exhibits two distinct superconducting domes (SC I and SC II) with increasing Ti doping. Clear de Haas–van Alphen (dHvA) oscillations were observed in all samples. At low Ti content ($x = 0.03$), corresponding to the SC I dome, a rich frequency spectrum (nine distinct peaks) was observed, which decreases to four peaks at $x = 0.15$, corresponding to the SC II dome. The change in the frequency spectrum strongly supports a significant modification of the Fermi surface topology and electronic structure in CsV_3Sb_5.

DFT calculations support these observations, showing that Ti substitution modifies the Fermi surface topology and electronic structure, including band shifts and key features such as flat bands, Dirac points, and van Hove singularities near the Fermi level. The evolution of the electronic structure with Ti doping follows a trend similar to that observed in our recent studies under hydrostatic pressure [42,63] in CsV_3Sb_5, indicating that this material is highly sensitive to pressure.

The combined experimental and theoretical results demonstrate that Ti doping induces significant modifications to the Fermi surface, consistent with the emergence of two superconducting domes with distinct pairing symmetries in $CsTi_xV_{3-x}Sb_5$. These findings suggest that the interplay among Fermi surface topology, disorder, and electronic correlations plays a crucial role in determining the pairing mechanisms across the two superconducting regions.

ACKNOWLEDGMENTS

This work was supported in part by the U.S. Department of Energy, Office of Science, Office of Workforce Development for Teachers and Scientists (WDTS) under the Visiting Faculty Program (VFP) at Los Alamos National Laboratory, administered by the Oak Ridge Institute for Science and Education. The work at West Texas A&M University (WTAMU) was supported by the Killgore Undergraduate and Graduate Student Research Grants, the Welch Foundation (Grant No. AE-0025), and the National Science Foundation (Award ID 2336011). Computations were performed on the WTAMU HPC cluster, funded by the National Science Foundation (NSF CC GROWTH 2018841). G.P. and M.J.S. gratefully acknowledge the support of the Dr. James "Earl" Perry CMCS Fund and the University of West Georgia. S.D.W. gratefully acknowledges support via the UC Santa Barbara NSF Quantum Foundry funded via the Q-AMASE-i program under Award No. DMR-1906325. A portion of this work was performed at the NHMFL, which is supported by National Science Foundation Cooperative Agreement No. DMR-2128556, the State of Florida, and the U.S. Department of Energy.

DATA AVAILABILITY

The data that support the findings of this article are not publicly available. The data are available from the authors upon reasonable request.

[1] J.-X. Yin, B. Lian, and M. Z. Hasan, Topological kagome magnets and superconductors, Nature (London) **612**, 647 (2022).

[2] S. D. Wilson and B. R. Ortiz, AV_3SB_5 kagome superconductors, Nat. Rev. Mater. **9**, 420 (2024).

[3] Y. Wang, H. Wu, G. T. McCandless, J. Y. Chan, and M. N. Ali, Quantum states and intertwining phases in kagome materials, Nat. Rev. Phys. **5**, 635 (2023).

[4] K. Shtefiienko, C. Phillips, S. Mozaffari, R. P. Madhogaria, W. R. Meier, D. G. Mandrus, D. E. Graf, and K. Shrestha, Electronic structure of YV_6Sn_6 probed by de Haas–van Alphen oscillations and density functional theory, APL Quantum **2**, 016118 (2025).

[5] K. Shtefiienko, C. Phillips, B. R. Ortiz, D. E. Graf, and K. Shrestha, Electronic structure of the kagome metal $YbTi_3Bi_4$ studied using torque magnetometry, Phys. Rev. B **111**, 035145 (2025).

[6] G. Pokharel, Samuel M. L. Teicher, B. R. Ortiz, P. M. Sarte, G. Wu, S. Peng, J. He, R. Seshadri, and S. D. Wilson, Electronic properties of the topological kagome metals YV_6Sn_6 and GdV_6Sn_6, Phys. Rev. B **104**, 235139 (2021).

[7] J. Lee and E. Mun, Anisotropic magnetic property of single crystals RV_6Sn_6 (R = Y, Gd-Tm, Lu), Phys. Rev. Mater. **6**, 083401 (2022).

[8] B. R. Ortiz, L. C. Gomes, J. R. Morey, M. Winiarski, M. Bordelon, J. S. Mangum, I. W. Oswald, J. A. Rodriguez-Rivera, J. R. Neilson, S. D. Wilson, E. Ertekin, T. M. McQueen, and E. S. Toberer, New kagome prototype materials: Discovery of KV_3Sb_5, RbV_3Sb_5, and CsV_3Sb_5, Phys. Rev. Mater. **3**, 094407 (2019).

[9] B. R. Ortiz, S. M. Teicher, Y. Hu, J. L. Zuo, P. M. Sarte, E. C. Schueller, A. M. Abeykoon, M. J. Krogstad, S. Rosenkranz, R. Osborn, R. Seshadri, L. Balents, J. He, and S. D. Wilson, CSV_3Sb_5: A $\mathbb{Z}_2$ Topological kagome metal with a superconducting ground state, Phys. Rev. Lett. **125**, 247002 (2020).

[10] Hasitha W. S. Arachchige, W. R. Meier, M. Marshall, T. Matsuoka, R. Xue, M. A. McGuire, R. P. Hermann, H. Cao, and D. Mandrus, Charge density wave in kagome lattice intermetallic ScV_6Sn_6, Phys. Rev. Lett. **129**, 216402 (2022).

[11] D. Werhahn, B. R. Ortiz, A. K. Hay, S. D. Wilson, R. Seshadri, and D. Johrendt, The kagome metals $CsTi_3Bi_5$ and $RbTi_3Bi_5$, Z. Naturforsch. B **77**, 757 (2022).

[12] B. R. Ortiz, H. Miao, D. S. Parker, F. Yang, G. D. Samolyuk, E. M. Clements, A. Rajapitamahuni, T. Yilmaz, E. Vescovo, J. Yan, *et al.*, Evolution of highly anisotropic magnetism in the titanium-based kagome metals $LnTi_3Bi_4$ (Ln: LA $\cdots$ Gd^{3+}, Eu^{2+}, Yb^{2+}), Chem. Mater. **35**, 9756 (2023).

[13] B. R. Ortiz, H. Zhang, K. Górnicka, D. S. Parker, G. D. Samolyuk, F. Yang, H. Miao, Q. Lu, R. G. Moore, A. F. May, *et al.*, Intricate magnetic landscape in antiferromagnetic kagome metal $TbTi_3Bi_4$ and interplay with $Ln_{2-x}Ti_{6+x}Bi_9$ (Ln: Tb $\cdots$ Lu) Shurikagome Metals, Chem. Mater. **36**, 8002 (2024).

[14] C. Phillips, K. Shtefiienko, S. Mozaffari, R. P. Madhogaria, W. R. Meier, A. F. Savvidou, B. W. Casas, L. Balicas, D. G. Mandrus, D. E. Graf, *et al.*, Electrical transport and torque magnetometry studies of the kagome compound LuV_6Sn_6 under high magnetic fields, Phys. Rev. B **111**, 155136 (2025).

[15] K. Shrestha, R. Chapai, B. K. Pokharel, D. Miertschin, T. Nguyen, X. Zhou, D. Y. Chung, M. G. Kanatzidis, J. F. Mitchell, U. Welp, D. Popovic, D. E. Graf, B. Lorenz, and W. K. Kwok, Nontrivial fermi surface topology of the kagome superconductor CsV_3Sb_5 probed by de Haas–van alphen oscillations, Phys. Rev. B **105**, 024508 (2022).

[16] K. Shrestha, M. Shi, T. Nguyen, D. Miertschin, K. Fan, L. Deng, D. E. Graf, X. Chen, and C.-W. Chu, Fermi surface mapping of the kagome superconductor RbV_3Sb_5 using de Haas-van Alphen oscillations, Phys. Rev. B **107**, 075120 (2023).

[17] K. Shrestha, M. Shi, B. Regmi, T. Nguyen, D. Miertschin, K. Fan, L. Z. Deng, N. Aryal, S.-G. Kim, D. E. Graf, X. Chen, and C. W. Chu, High quantum oscillation frequencies and nontrivial topology in kagome superconductor KV_3Sb_5 probed by torque magnetometry up to 45 T, Phys. Rev. B **107**, 155128 (2023).

[18] S. R. Bhandari, M. Zeeshan, V. Gusain, K. Shrestha, and D. Rai, First-principles study of the electronic structure, Z_2 invariant, and quantum oscillation in the kagome material CsV_3Sb_5, APL Quantum **1**, 046118 (2024).

[19] W. Zhang, L. Wang, C. W. Tsang, X. Liu, J. Xie, W. C. Yu, K. T. Lai, and S. K. Goh, Emergence of large quantum oscillation frequencies in thin flakes of the kagome superconductor CsV_3Sb_5, Phys. Rev. B **106**, 195103 (2022).

[20] D. Chen, B. He, M. Yao, Y. Pan, H. Lin, W. Schnelle, Y. Sun, J. Gooth, L. Taillefer, and C. Felser, Anomalous thermoelectric effects and quantum oscillations in the kagome metal CsV_3Sb_5, Phys. Rev. B **105**, L201109 (2022).

[21] C. Broyles, D. Graf, H. Yang, X. Dong, H. Gao, and S. Ran, Effect of the interlayer ordering on the fermi surface of kagome superconductor CsV_3Sb_5 revealed by quantum oscillations, Phys. Rev. Lett. **129**, 157001 (2022).

[22] Z. Wang, W. Zhang, L. Wang, T. F. Poon, C. W. Tsang, W. Wang, J. Xie, S. T. Lam, X. Zhou, Y. Zhao, *et al.*, Similarities and differences in the fermiology of kagome metals AV_3Sb_5 (A = K, Rb, Cs) revealed by shubnikov–de haas oscillations, Appl. Phys. Lett. **123**, 012601 (2023).

[23] Z. Liang, X. Hou, F. Zhang, W. Ma, P. Wu, Z. Zhang, F. Yu, J.-J. Ying, K. Jiang, L. Shan, *et al.*, Three-dimensional charge density wave and surface-dependent vortex-core states in a kagome superconductor CsV_3Sb_5, Phys. Rev. X **11**, 031026 (2021).

[24] B. Lorenz and C. Chu, High pressure effects on superconductivity, in *Frontiers in Superconducting Materials* (Springer, Berlin, 2005), pp. 459–497.

[25] M. Xu, Y. Li, and Y. Ma, Materials by design at high pressures, Chem. Sci. **13**, 329 (2022).

[26] A. Dewaele and L. Nataf, Magnetic phase diagram of iron at high pressure and temperature, Phys. Rev. B **106**, 014104 (2022).

[27] I. Levatić, P. Popčević, V. Šurija, A. Kruchkov, H. Berger, A. Magrez, J. S. White, H. M. Rønnow, and I. Živković, Dramatic pressure-driven enhancement of bulk skyrmion stability, Sci. Rep. **6**, 21347 (2016).

[28] L. Deng, H.-C. Wu, A. P. Litvinchuk, N. F. Yuan, J.-J. Lee, R. Dahal, H. Berger, H.-D. Yang, and C.-W. Chu, Room-temperature skyrmion phase in bulk Cu_2OSeO_3 under high pressures, Proc. Natl. Acad. Sci. USA **117**, 8783 (2020).

[29] H. Takahashi, A. Sugimoto, Y. Nambu, T. Yamauchi, Y. Hirata, T. Kawakami, M. Avdeev, K. Matsubayashi, F. Du, C. Kawashima, *et al.*, PRessure-induced superconductivity in the iron-based ladder material $BaFe_2S_3$, Nat. Mater. **14**, 1008 (2015).

[30] J. Zhang, S. Zhang, H. Weng, W. Zhang, L. Yang, Q. Liu, S. Feng, X. Wang, R. Yu, L. Cao, *et al.*, Pressure-induced su-

perconductivity in topological parent compound Bi_2Te_3, Proc. Natl. Acad. Sci. USA **108**, 24 (2011).

[31] K. Shrestha, L. Deng, K. Zhao, B. Jawdat, B. Lv, B. Lorenz, and C. Chu, Doping dependence and high-pressure studies on $Eu_xCa_{1-x}Fe_2As_2 (0 \leqslant x \leqslant 1)$, Supercond. Sci. Technol. **33**, 095010 (2020).

[32] J. Hou, K. Y. Chen, J. P. Sun, Z. Zhao, Y. H. Zhang, P. F. Shan, N. N. Wang, H. Zhang, K. Zhu, Y. Uwatoko, H. Chen, H. T. Yang, X. L. Dong, H. J. Gao, and J. G. Cheng, Effect of hydrostatic pressure on the unconventional charge density wave and superconducting properties in two distinct phases of doped kagome superconductors $CsV_{3-x}Ti_xSb_5$, Phys. Rev. B **107**, 144502 (2023).

[33] H. Yang, Z. Huang, Y. Zhang, Z. Zhao, J. Shi, H. Luo, L. Zhao, G. Qian, H. Tan, B. Hu, *et al.*, Titanium Doped kagome superconductor $CsV_{3-x}Ti_xSb_5$ and two distinct phases, Sci. Bull. **67**, 2176 (2022).

[34] K. J. Zhu, L. P. Nie, B. Lei, M. J. Wang, K. L. Sun, Y. Z. Deng, M. L. Tian, T. Wu, and X. H. Chen, Competitive superconductivity and charge density wave in mo-doped kagome superconductor CsV_3Sb_5, Phys. Rev. Res. **6**, 023295 (2024).

[35] S. Yousuf, J. Song, H. Jang, V. T. A. Hong, T. Lee, N. ul Ain, S. YH, Y. Kim, H. Lee, and T. Park, Synthesis and physical properties of cr-doped kagome superconductor CsV_3Sb_5, Curr. Appl. Phys. **61**, 7 (2024).

[36] F. Song, C. Ke, Y. Liu, T. Weng, C.-C. Hsieh, C. H. Cheng, Y. Chen, and Y. Zhao, Effect of sulfur doping on superconductivity and charge density wave order in kagome metal $CsV_3(Sb_{1-x}S_x)_5$, Supercond. Sci. Technol. **38**, 015010 (2025).

[37] Y. Liu, Y. Wang, Y. Cai, Z. Hao, X.-M. Ma, L. Wang, C. Liu, J. Chen, L. Zhou, J. Wang, *et al.*, Doping evolution of superconductivity, charge order, and band topology in hole-doped topological kagome superconductors $Cs(V_{1-x}Ti_x)_3Sb_5$, Phys. Rev. Mater. **7**, 064801 (2023).

[38] Y. M. Oey, B. R. Ortiz, F. Kaboudvand, J. Frassineti, E. Garcia, R. Cong, S. Sanna, V. F. Mitrović, R. Seshadri, and S. D. Wilson, Fermi level tuning and double-dome superconductivity in the kagome metal $CsV_3Sb_{5-x}Sn_x$, Phys. Rev. Mater. **6**, L041801 (2022).

[39] G. Pokharel, C. Zhang, E. Redekop, B. R. Ortiz, A. N. Salinas, S. Schwarz, S. J. G. Alvarado, S. Sarker, A. F. Young, and S. D. Wilson, Evolution of charge correlations in the hole-doped kagome superconductor $CsV_{3-x}Ti_xSb_5$, Phys. Rev. Mater. **9**, 094805 (2025).

[40] F. Yu, D. Ma, W. Zhuo, S. Liu, X. Wen, B. Lei, J. Ying, and X. Chen, Unusual competition of superconductivity and charge-density-wave state in a compressed topological kagome metal, Nat. Commun. **12**, 3645 (2021).

[41] K. Y. Chen, N. N. Wang, Q. W. Yin, Y. H. Gu, K. Jiang, Z. J. Tu, C. S. Gong, Y. Uwatoko, J. P. Sun, H. C. Lei, J. P. Hu, and J. G. Cheng, Double superconducting dome and triple enhancement of T_c in the kagome superconductor CsV_3Sb_5 under high pressure, Phys. Rev. Lett. **126**, 247001 (2021).

[42] C. Phillips, K. Shtefiienko, T. Nguyen, A. N. Capa Salinas, B. A. Magar, G. Pokharel, S. D. Wilson, D. E. Graf, and K. Shrestha, Fermi surface reconstruction under pressure in the kagome metal CsV_3Sb_5, Phys. Rev. B **110**, 205135 (2024).

[43] S. Peng, Y. Han, G. Pokharel, J. Shen, Z. Li, M. Hashimoto, D. Lu, B. R. Ortiz, Y. Luo, H. Li, *et al.*, Realizing kagome band structure in two-dimensional kagome surface states of RV_6Sn_6 (R = Gd, Ho), Phys. Rev. Lett. **127**, 266401 (2021).

[44] E. Rosenberg, J. M. DeStefano, Y. Guo, J. S. Oh, M. Hashimoto, D. Lu, R. J. Birgeneau, Y. Lee, L. Ke, M. Yi, *et al.*, Uniaxial ferromagnetism in the kagome metal TbV_6Sn_6, Phys. Rev. B **106**, 115139 (2022).

[45] K. Shrestha, B. Regmi, G. Pokharel, S.-G. Kim, S. D. Wilson, D. E. Graf, B. A. Magar, C. Phillips, and T. Nguyen, Electronic properties of kagome metal ScV_6Sn_6 using high-field torque magnetometry, Phys. Rev. B **108**, 245119 (2023).

[46] L. Kautzsch, Y. M. Oey, H. Li, Z. Ren, B. R. Ortiz, G. Pokharel, R. Seshadri, J. Ruff, T. Kongruengkit, J. W. Harter, *et al.*, Incommensurate charge-stripe correlations in the kagome superconductor $CsV_3Sb_{5-x}Sn_x$, npj Quantum Mater. **8**, 37 (2023).

[47] K. Shtefiienko, C. Phillips, M. J. Stitz, G. Pokharel, S. D. Wilson, D. E. Graf, and K. Shrestha, Pressure effects on the fermi surface of Ti-doped CsV_3Sb_5, Phys. Rev. B **111**, 235135 (2025).

[48] P. Blaha, K. Schwarz, F. Tran, R. Laskowski, G. K. Madsen, and L. D. Marks, Wien2k: An apw+ lo program for calculating the properties of solids, J. Chem. Phys. **152**, 074101 (2020).

[49] P. Blaha, K. Schwarz, G. K. Madsen, D. Kvasnicka, J. Luitz, *et al.*, Wien2k, An augmented plane wave+ local orbitals program for calculating crystal properties **60** (2001).

[50] P. Giannozzi, S. Baroni, N. Bonini, M. Calandra, R. Car, C. Cavazzoni, D. Ceresoli, G. L. Chiarotti, M. Cococcioni, I. Dabo, *et al.*, QUANTUM ESPRESSO: A modular and open-source software project for quantum simulations of materials, J. Phys.: Condens. Matter **21**, 395502 (2009).

[51] P. Giannozzi, O. Andreussi, T. Brumme, O. Bunau, M. B. Nardelli, M. Calandra, R. Car, C. Cavazzoni, D. Ceresoli, M. Cococcioni, *et al.*, Advanced capabilities for materials modeling with QUANTUM ESPRESSO, J. Phys.: Condens. Matter **29**, 465901 (2017).

[52] P. Giannozzi, O. Baseggio, P. Bonfà, D. Brunato, R. Car, I. Carnimeo, C. Cavazzoni, S. De Gironcoli, P. Delugas, F. Ferrari Ruffino, *et al.*, QUANTUM ESPRESSO toward the exascale, J. Chem. Phys. **152**, 154105 (2020).

[53] J. P. Perdew, K. Burke, and M. Ernzerhof, Generalized gradient approximation made simple, Phys. Rev. Lett. **77**, 3865 (1996).

[54] S. Julian, Numerical extraction of de Haas–van alphen frequencies from calculated band energies, Comput. Phys. Commun. **183**, 324 (2012).

[55] K. Fukushima, K. Obata, S. Yamane, Y. Hu, Y. Li, Y. Yao, Z. Wang, Y. Maeno, and S. Yonezawa, Violation of emergent rotational symmetry in the hexagonal kagome superconductor CsV_3Sb_5, Nat. Commun. **15**, 2888 (2024).

[56] W. Zhang, X. Liu, L. Wang, C. W. Tsang, Z. Wang, S. T. Lam, W. Wang, J. Xie, X. Zhou, Y. Zhao, *et al.*, Nodeless superconductivity in kagome metal CsV_3Sb_5 with and without time reversal symmetry breaking, Nano Lett. **23**, 872 (2023).

[57] K. Jiang, T. Wu, J.-X. Yin, Z. Wang, M. Z. Hasan, S. D. Wilson, X. Chen, and J. Hu, Kagome superconductors AV_3Sb_5 (A = K, Rb, Cs), Natl. Sci. Rev. **10**, nwac199 (2023).

[58] B. R. Ortiz, S. M. Teicher, L. Kautzsch, P. M. Sarte, N. Ratcliff, J. Harter, J. P. Ruff, R. Seshadri, and S. D. Wilson, Fermi surface mapping and the nature of charge-density-wave order in the kagome superconductor CsV_3Sb_5, Phys. Rev. X **11**, 041030 (2021).

[59] F. H. Yu, T. Wu, Z. Y. Wang, B. Lei, W. Z. Zhuo, J. J. Ying, and X. H. Chen, Concurrence of anomalous Hall effect and charge density wave in a superconducting topological kagome metal, Phys. Rev. B **104**, L041103 (2021).

[60] Q. Yin, Z. Tu, C. Gong, Y. Fu, S. Yan, and H. Lei, Superconductivity and normal-state properties of kagome metal RbV_3Sb_5 single crystals, Chin. Phys. Lett. **38**, 037403 (2021).

[61] Y. Fu, N. Zhao, Z. Chen, Q. Yin, Z. Tu, C. Gong, C. Xi, X. Zhu, Y. Sun, K. Liu, *et al.*, Quantum transport evidence of topological band structures of kagome superconductor CsV_3Sb_5, Phys. Rev. Lett. **127**, 207002 (2021).

[62] Y. Ando, Topological insulator materials, J. Phys. Soc. Jpn. **82**, 102001 (2013).

[63] S. R. Bhandari, V. Gusain, M. Zeeshan, D. Rai, and K. Shrestha, Pressure effects on the electronic structure of the kagome metal CsV_3Sb_5, APL Quantum **2**, 016133 (2025).

[64] D. Shoenberg, *Magnetic Oscillations in Metals* (Cambridge University Press, Cambridge, 2009).

[65] C. Kittel and P. McEuen, *Introduction to Solid State Physics* (John Wiley & Sons, New York, 2018).

[66] K. Shrestha, V. Marinova, B. Lorenz, and P. C. Chu, SHubnikov-de Haas oscillations from topological surface states of metallic $Bi_2Se_{2.1}Te_{0.9}$, Phys. Rev. B **90**, 241111(R) (2014).

[67] M. Kang, S. Fang, J.-K. Kim, B. R. Ortiz, S. H. Ryu, J. Kim, J. Yoo, G. Sangiovanni, D. Di Sante, B.-G. Park, *et al.*, Twofold van hove singularity and origin of charge order in topological kagome superconductor CsV_3Sb_5, Nat. Phys. **18**, 301 (2022).

[68] K. Shtefiienko, S. Zhang, U. A. de la Sierra, G. Pokharel, and K. Shrestha, Superconducting properties of the Ti-doped KV_3Sb_5 kagome compound, Phys. Rev. B **112**, 115140 (2025).